# Boundary Layer Thermodynamics of a High Plains Severe Storm

ALAN K. BETTS[1]

*West Pawlet, VT 05775*

(Manuscript received 2 September 1983, in final form 21 June 1984)

ABSTRACT

A new analysis method based on air parcel saturation point is used to intercompare data sampled by different systems (aircraft, rawinsondes, and a surface mesonet) during the passage of one severe storm in the 1981 Cooperative Convective Precipitation Experiment. The low-level thermodynamic structure simplifies into two distinct branches on a thermodynamic diagram. The lower tropospheric environment ahead of the severe storm has a characteristic mixing line structure while the storm low-level outflow has a distinct evaporation line structure.

## 1. Introduction

In this paper the bulk thermodynamics associated with a severe cumulonimbus system are analyzed: in particular its inflow and outflow in the lowest few hundred millibars. A relatively new analysis technique using air parcel saturation point (Betts, 1982a,b) is used to simplify the thermodynamic analysis in terms of conserved parameters and simultaneously compact data from surface and aircraft (sampled at different levels) into comparable form. This study also draws on the conceptual analysis of downdrafts in terms of mixing and evaporative processes suggested by Betts (1976b). The data used comes from the 1981 Cooperative Convective Precipitation Experiment (CCOPE). This experiment was designed to study convective clouds and storms over a network near Miles City, Montana, using a dense surface mesonetwork, upper air soundings from five stations, 14 research aircraft and seven Doppler radars (Knight, 1982). The mesoscale thermodynamic structure associated with a severe storm, which passed through the research area on 1 August, 1981, is analyzed. The environment of High Plains thunderstorms is complex; with large horizontal gradients of moisture at the surface and large gradients in the vertical. On 1 August 1981 conditions occurred that were favorable for severe weather with a deep mixed layer of high $\theta$ and low $\theta_E$ (continental tropical air) overlying a slightly cooler mixed layer of moister air (for example, see Ludlam, 1963, 1980; Knight and Squires, 1982; Carlson and Ludlam, 1968; Carlson *et al.*, 1983). Downdrafts produced surface winds exceeding 50 knots; large hail occurred at the surface, and one aircraft suffered serious hail damage. This vigorous overturning is related to the near neutrality (in virtual potential temperature) of the vertical atmospheric structure and to the large difference in $\theta_E$ between the two overlying layers, in the presence of large-scale shear (Browning and Ludlam, 1962). Downdrafts behind the surface gust-front transform the boundary layer (Charba, 1974; Goff, 1976), similar to the transformation observed for tropical systems (Zipser, 1969, 1977; Betts, 1976b).

In part, this paper is simply a new presentation for the familiar thermodynamic environment common to severe storms. However, the saturation point method has several advantages as an analysis tool in the study of thunderstorm thermodynamics:

i) The method simplifies the analysis of data collected by horizontal and vertical spatial sampling and single station time series by different systems: aircraft, upper air soundings and the surface mesonet.

ii) It compacts the cloud and mesoscale thunderstorm thermodynamics into two basic branches on a saturation point diagram (Betts, 1982a): a *mixing line* and an *evaporation line.* This permits a clear physical separation between the different processes of vertical mixing and the evaporation of precipitation. The slope of the mixing line is related directly to the vertical gradient of virtual potential temperature so that changes in stability associated with advection and the conditioning of the prestorm boundary layer are readily visible.

iii) The SP formulation suggests methods for the budget analysis of the subcloud layer using time-series aircraft data just below cloud base, together with surface data.

[1] Visiting Scientist, Convective Storms Division, National Center for Atmospheric Research, Boulder, CO 80307. NCAR is sponsored by the National Science Foundation.

© 1984 American Meteorological Society

## 2. Saturation point thermodynamics

This system was introducted by Betts (1982a) and extended in Betts (1982b, 1983) to represent compactly the thermodynamics of moist air using air parcel saturation point (SP). Formally the SP of an unsaturated (cloudy) air parcel is found by dry (moist) adiabatic ascent (descent) to the pressure level where the parcel is just saturated (with no cloud liquid water content) (Betts, 1982a). At this saturation level (SL), the parcel temperature and pressure ($T_{SL}$, $p_{SL}$) uniquely specify the conserved parcel thermodynamic parameters (Betts, 1973). For unsaturated air these are ($\theta$, $\theta_E$, $q$) and for cloudy air ($\theta_L$, $\theta_{ES}$, $q_T$), where $\theta_{(L)}$ denotes (liquid water) potential temperature, $\theta_{E(S)}$ (saturation) equivalent potential temperature, $q_{(S)}$ (saturation) water vapor mixing ratio, $q_T = q_S + l$ total water and $l$ cloud water (carried with air parcels until precipitated).

In this paper we shall deal almost entirely with measurements made in unsaturated environmental air, so that the SP is the $T$, $p$ at the familiar lifting condensation level of an air parcel on a thermodynamic diagram. When air parcels of different SP are mixed together in the absence of precipitation, the SP of different mixtures lie along a well-defined mixing line joining the SP of the two parcels (Betts, 1982a). Paluch (1979) showed how these mixing lines can be drawn on conserved parameter diagrams. She used a modified $\theta_E$ and total water. The advantage of the SP diagram is that it is a construction on a conventional thermodynamic diagram, which simultaneously shows all three conserved parameter fields. In addition the virtual potential temperature isopleths can be added (Betts, 1982a) to facilitate comparisons of air parcel buoyancy. Although in principle, all the isopleths (of $T$, $p$, $\theta_L$, $\theta_V$ at air parcel saturation level) could be added to a Paluch diagram, the resulting chart is less convenient than the familiar thermodynamic chart.

We shall see in Section 5 numerous examples of this mixing line structure before the onset of precipitation. The evaporation of falling precipitation into unsaturated air moves the air parcel SP down the moist adiabat (changing $\theta$ and $q$ but approximately conserving $\theta_E$). We shall find in Section 6 that air parcels that have been modified by evaporation of falling precipitation have SP which scatter close to a $\theta_E$ isopleth, and we shall describe this as an *evaporation line* structure.

## 3. Data sources

### a. Surface mesonet data

Figure 1 shows the location of the sites in the CCOPE radar network and the dense surface mesonetwork. The long-dashed line shows the perimeter of the Doppler radar network and the short-dashed line the interior triangle formed by the NOAA-WPL

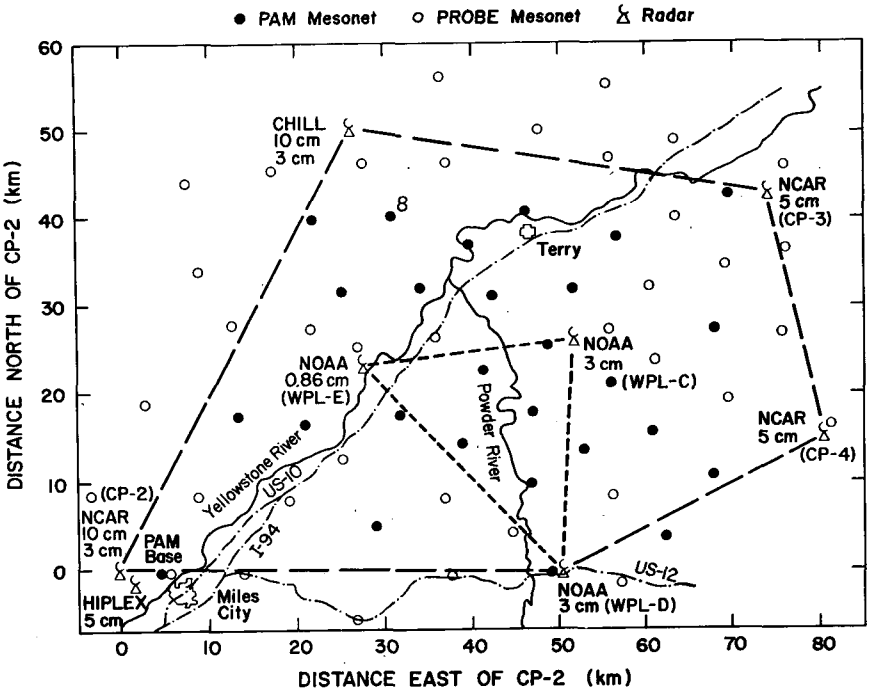


FIG. 1. The primary CCOPE operation area was within the Doppler radar network, which coincided with the dense mesonet, both shown here. The operations center was at CP-2 radar site at the origin of the coordinate system, near Miles City and its airport (from Knight, 1982).

radars. The headquarters of the project was the Miles City Airport, located across the Yellowstone River from Miles City, where the PAM Base is indicated. The surface mesonetwork was a mixture of two systems. The Portable Automated Mesonet (PAM) of NCAR's Field Observing Facility consisted of 27 stations that collected one-minute-average data, telemetered every minute to the PAM base, where they were immediately accessible through computer terminals. The new Portable Remote Observation of the Environment (PROBE) system, developed by the Bureau of Reclamation and operated by the Montana State Department of Natural Resources, collected five-minute-average data, which were transmitted to a satellite every hour (and retrievable within an hour) from 96 surface stations in a larger network. The location of aircraft observations or soundings will be expressed in km using the $(x, y)$ coordinates shown in Fig. 1.

### *b. Aircraft data*

We shall use aircraft data primarily from two CCOPE aircraft: the Wyoming King Air, and the NCAR Queen Air N306D.

### *c. Sounding data*

The principal sounding network was not operating on this day and only three soundings (at 0600, 1400, and 1700 MDT) of low vertical resolution (significant levels) are available from Miles City.

## 4. Meteorological situation on 1 August 1981

Southeasterly surface winds (shifting to southerly during the afternoon) brought in moist air beneath an unstable sounding aloft (Fig. 3) and cumulonimbus developed rapidly. The storms were severe, producing large hail and surface gusts exceeding 25 m $s^{-1}$. Figure 2 shows a schematic of the radar echoes (>30 dBZ) (composited from the Bureau of Reclamation Skywater radar and the NCAR CP-2 radar) and the outflow boundary as it crossed the surface mesonet. The area shown in Fig. 2 is that of the larger scale PROBE mesonet (the pentagonal outline of the radar network in Fig. 1 is shown dashed). The major severe storm developed to the north of the PAM mesonet and propagated towards the southeast: its outflow boundary is marked as it swept across the mesonet. A smaller system grew in the east of the PAM mesonet (1600 MDT) and then decayed. A new cumulonimbus in the PAM network grew at 1800 MDT, and merged with the major system by 1900 MDT.

A convergence zone with an associated horizontal gradient of moisture extends north–south through the mesonet: Fig. 6, (shown later), shows an example of the surface fields as the gust front crosses the dense mesonet.

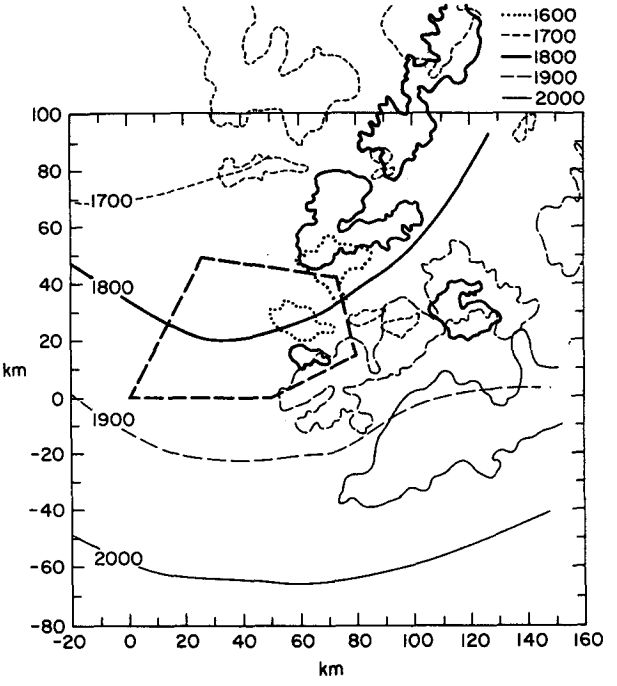


FIG. 2. Area of larger scale PROBE mesonet, with radar echoes (>30 dBZ) shown at hourly intervals (MDT) and position of surface gust front as it crosses the network.

## 5. Thermodynamic structure before precipitation

### *a. Vertical sounding structure*

Figure 3 shows two soundings made by the Wyoming King Air over the dense mesonet in the inflow region to the storm system. The first (heavy line–solid circles) is near 1440 MDT with approximate coordinates (+30, +10 km) (see Fig. 1), the second near 1610 MDT at a similar location (light lines, open circles). The circles denote the SP for representative sounding levels. The heavy dashed line is the mixing line drawn between an SP of 10.1°C, 706 mb corresponding to subcloud layer air at 1440 MDT, and −17°C, 473 mb corresponding to the SP of air in the upper nearly adiabatic layer between 650 and 550 mb. All of the sounding SP lie close to this mixing line. The temperature and moisture structure of the two King Air soundings are consistent with subsidence near 500 mb between 1440 and 1610 MDT. However, neither air parcel SP nor the mixing line are affected by adiabatic sinking. The Miles City sounding at 1700 MDT is further to the west and has a drier mixed layer, but its SP (symbol M) still lie on the same mixing line.

The dotted line is the virtual potential temperature isopleth for unsaturated air $\theta_{vu}$ = 315 K (Betts, 1982a) through the cloud-base SP. The mixing line lies above it, as is necessary for the atmosphere to be stable to dry overturning (Betts, 1982a), but not much above it, indicating the extreme instability of the atmosphere

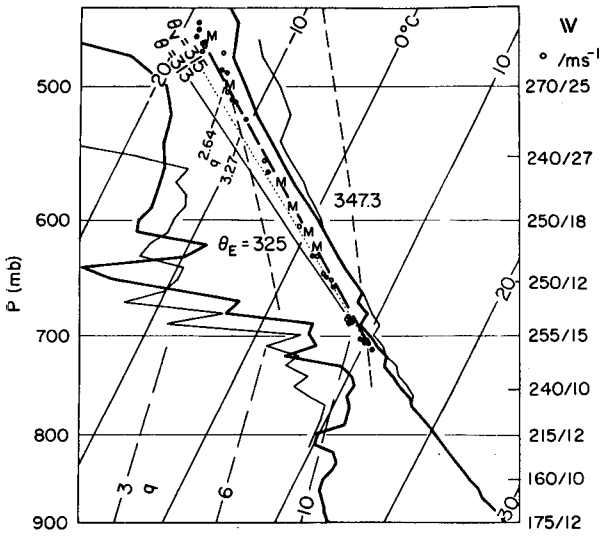


FIG. 3. Soundings by Wyoming King Air on a skew $T$–log$p$ diagram at 1435–1450 MDT [showing ($T$, $T_D$) as heavy lines and SP as solid circles] and 1605–1616 MDT (light lines and open circles). Heavy dashed line is mixing line between subcloud layer and drier air (550–650 mb) aloft. M denotes SP of Miles City sounding at 1700 MDT. Dotted line is $\theta_{vu}$ = 315 K isopleth through cloud base SP.

to moist convection. The evaporation of cumulus towers which have not precipitated their liquid water content will produce temperatures on this mixing line, and these mixtures can sink towards the stable layer at cloud base (710 mb), but not into the subcloud layer. However the evaporation of a little precipitation into the dry layer will easily lower $\theta_v$ so as to produce downdrafts to the surface. The $\theta_E$ = 325 K line is drawn to indicate this. The evaporation of only 0.67 g kg$^{-1}$ liquid water into air with SP on the ML will move its SP down the 325 K $\theta_E$ isopleth and lower $\theta_{vu}$ to 315 K, sufficient to penetrate the stable layer near cloud-base (see Section 6d).

### *b. Structure below cloud base*

The NCAR Queen Air (N306D) made two flights covering the time period from 1400 to 2030 MDT mostly at a flight level just below cloud base in the inflow region ahead of the storm, followed by soundings through the storm gust front in the final half-hour. This long time series near cloud base shows the evolution of the thermodynamics of the inflow region and is shown in Fig. 4. While flying at one pressure altitude, the plane samples air from the subcloud layer interspersed with pockets of warmer, drier, lower $\theta_E$ air which have descended dry adiabatically from above cloud-base. Thus, the flight level data give a similar mixing line structure on an SP diagram as a vertical sounding. Figure 4 shows the time evolution of this mixing line (ML) through the afternoon. The stratification of all the data along a well-defined mixing line indicates that only mixing between the subcloud layer and the cumulus layer above has taken place (Betts, 1982a) in this air. The evaporation of precipitation moves SP off this ML and generates a different structure (see Section 6).

Figure 4 shows several important features:

i) For each time period, the aircraft data stratify along a well-defined ML, which is shifting in time (see iii).

ii) The change of cloud-base SP, and of the mixed layer with time can be estimated from the lower right end of the ML, as the vector ABC.

iii) Mixing lines constructed from points A, B, C and the early SP of the layer above (top of heavy dashed line in Fig. 3) are shown as dashed lines. They fit the data well, indicating that the dominant process during this time period is probably the change of subcloud SP A to C. There may also be smaller changes in the SP of the upper dry layer, but we neglect these since they are not well-defined by the aircraft soundings.

iv) Corresponding to the change of subcloud SP, A to C, towards larger $\theta_{vu}$ the ML rotates until by 1915 MDT it is parallel to $\theta_v$ = 316.8 K. This means that the initial stabilization above cloud base has

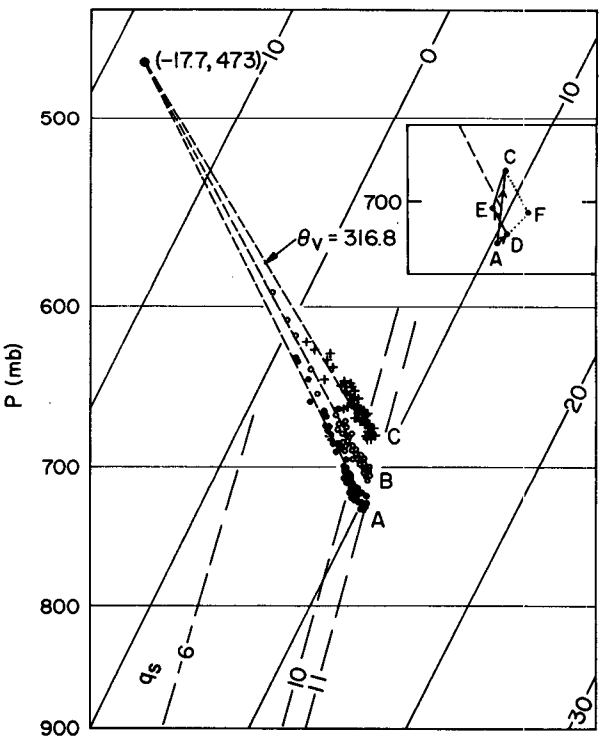


FIG. 4. Saturation points (SP) of air just below cloud base corresponding to three time periods: 1430–1530 MDT (solid), 1530–1630 (open circles), and 1845–1945 (crosses), showing change of mixing line structure with time. Data points are 1 s values every minute (duplicate values omitted) plotted on a section of a skew $T$–log$p$ diagram.

been eliminated, and the atmosphere has approached the marginal instability condition for dry overturning. It is possible that the whole layer from the surface to 550 mb then becomes rapidly mixed in some regions near the approaching storm (see Section 6d).

### c. *Subcloud layer budget*

Figure 4 shows some of the information necessary for the subcloud layer thermodynamic budget. Each set of aircraft data shows a distinct mixing line, which has a trend in time. The trend ABC of the extremum values (coolest and moistest SP) may be taken as the trend of the subcloud layer mean SP(M) with time. The fluxes through cloud base associated with the ascent of moist air and the mixing down of drier air from above would move M up the mixing line. This is not the trend observed so the surface fluxes and horizontal advection must play an important role in the budget.

One can formulate this heat and moisture budget of the subcloud layer as vectors on an SP diagram. This is of some formal interest, and is included as an appendix. However, without good estimates of the surface fluxes (which are not yet available for the CCOPE data), only a qualitative budget can be constructed. The insert to Fig. 4 shows a schematic budget (see appendix for details) by decomposing the vector trend of the subcloud SP (**AC**) into the sum of three vectors: **AD** for the estimated surface fluxes, **DE** for the convective fluxes through the cloud base, and **EC** associated with low level advection. Even this qualitative budget is sufficient to show the importance of low-level advection.

Because this diagram summarizes all the thermodynamic budgets in one figure, it also shows the separate effect of surface fluxes, cloud base fluxes, and advection in conditioning the mixed layer ahead of the storm, and is weakening the stable layer at cloud base. For example, the insert to Fig. 4 shows the subcloud $\theta_V$ is changed very little by the cloud-base fluxes (since **DE** is almost parallel to a $\theta_V$ isopleth) but a lot by horizontal advection. However, both processes are contributing significantly to the lifting of cloud base.

## 6. Thermodynamic structure produced by evaporation of precipitation

Before the onset of precipitation, the thermodynamic data are scattered along a well-defined mixing line, whose slope couples the convective fluxes above cloud-base. Further examples of this sturcture using surface mesonet data will be given in Section 6a. However, with the onset of precipitation, and its evaporation into unsaturated air (which drives downdrafts), a new characteristic *evaporation line* (EL) appears in the scatter of the SP. Evaporation lines

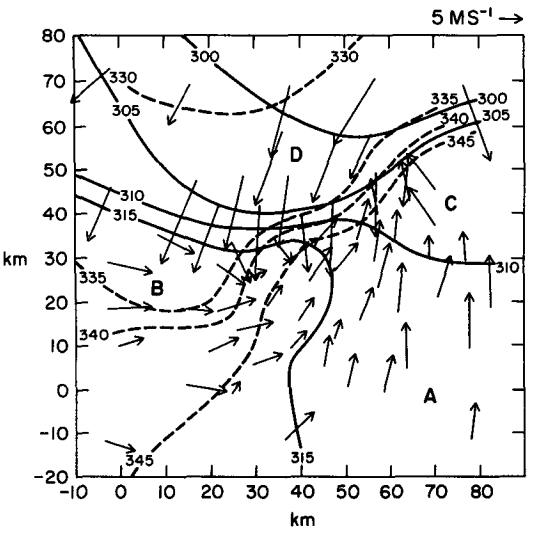


FIG. 5. Analysis of $\theta$, $\theta_E$ fields (K) of dense mesonet at 1745 MDT with superimposed wind vectors (data are 5 min averages preceding 1745).

are parallel to moist adiabats[2] and represent SP that result from different amounts of evaporation. Examples are given in this section using different data sources. Evaporation produces cooling, a lower $\theta_v$ and the downward transport of air in and from above the subcloud layer, until a complete restratification of the atmosphere results. Cold air of lower $\theta_E$ from cloud-scale downdrafts spreads over the surface, beneath mesoscale regions which have also been modified by precipitation and downdrafts. (Zipser, 1977; Miller and Betts, 1977).

### a. *Surface mesonet analysis*

To help interpret subsequent figures we show in Fig. 5 an analysis of 5 min averages of surface $\theta$ (solid lines), $\theta_E$ (dashed), together with surface wind vectors at 1745 MDT as the surface gust front covers nearly half the dense network (Fig. 1). Four regions are labelled with distinct properties. Region A is the southerly inflow of moist air with ($\theta$, $\theta_E$) of about (314, 347 K), region C is the same air modified by evaporation of showers (see evaporation line on Fig. 6a), region B is warm dry air further to the west with ($\theta$, $\theta_E$) of (316, 335 K), while region D is the major storm outflow of low ($\theta$, $\theta_E$) of typically (302, 333 K).

There is some scatter in the surface mesonet data from station to station but by plotting many stations the statistics of the population can be seen. We show in Figs. 6a, b and 7a, b the distribution of surface SP from the dense mesonet (Fig. 1) at hourly intervals from near the onset of the first shower until the

[2] We raise the possibility in Section 6f, that further study may show evaporation lines to be virtual $\theta_{ES}$ isopleths in some cases.

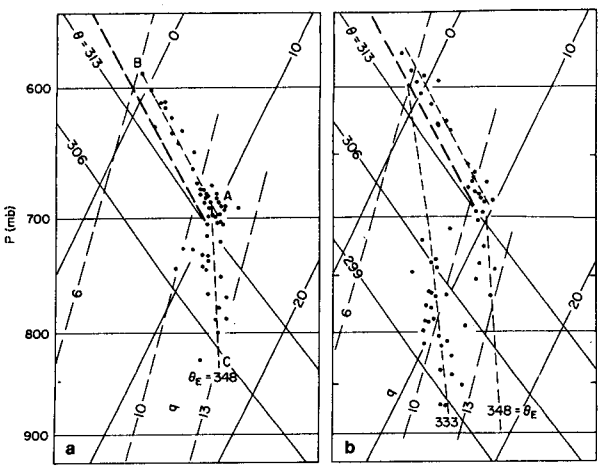


FIG. 6. SP plot of dense surface mesonet data at (a) 1700 and (b) 1800 MDT showing scatter along mixing line AB and evaporation line ($\theta_E \sim 348$ K) AC in (a), and two evaporation lines in (b), $\theta_E \sim 333$ K and 348 K.

severe storm system passes south–east of this network, and its outflow air has covered the mesonet.

Figure 6a shows the mesonet data at 1700 MDT. The surface SP scatter about two lines. One, AB, is a mixing line (light dashes) parallel to that (heavy dashes) of the mean sounding in Fig. 3 (the surface data, being in the superadiabatic layer, have a higher $\theta$ and $q$). The drier SP (towards B) correspond to surface air to the west which has entered the western part of the network (Fig. 5). The fact that the ML structure is essentially similar to that below cloud base in the storm inflow air (Fig. 4) and that of the vertical soundings (Fig. 3) implies that the dry continental air to the west at the surface is thermodynamically similar to the dry air overlying the moister inflow air. The interface between the two may indeed slope downward to the west to reach the surface.

The second line, AC, is an evaporation line (region C in Fig. 5). The evaporation of precipitation moves the SP of air parcels down a moist adiabat. The $\theta_E$ values of these SP are characteristic of the surface and subcloud values in the undisturbed air (344–351 K). These correspond to evaporation of precipitation into subcloud layer air in amounts from 1 to 3 g kg$^{-1}$. Only a few SP have lower $\theta_E$ values suggesting an origin near cloud base. This early storm downdraft thermodynamics differs markedly from the subsequent figures where we find lower and lower values of $\theta_E$, and $\theta$ at the surface, as the major storm system passes (Fig. 2) and brings downdraft air from higher in the atmosphere down to the surface (Figs. 7a, b).

Figure 6b shows the same plot of the surface mesonet SP an hour later at 1800 MDT. The gust front from the severe storm has entered the network (Fig. 5) although the southeast of the network still has high ($\theta$, $\theta_E$) inflow. The ML of unmodified surface air is unchanged, and there are still a few SP near $\theta_E$ = 348 K (see Fig. 6a). However the main gust front outflow has SP which scatter along an evaporation line, $\theta_E \sim 333$ K. These correspond to evaporation of 3 to 6 g kg$^{-1}$ of precipitation into air with an SP of −1°C, 600 mb with a ($\theta$, $q$, $\theta_E$) of 315 K, 6 g kg$^{-1}$, 333 K. Comparison with the King Air soundings in Fig. 3 shows that these thermodynamic properties do not correspond either to the subcloud moist air ($\theta_E \sim 347$ K) or to the dry continental air above ($\theta_E$ of 323 to 325 K), but rather to the transition between them just above cloud base. This and the subsequent Figs. 8, 9 raise the question of the source of the downdraft outflow air which is relatively homogeneous in $\theta_E$. Its $\theta_E$ suggests it originates from some mixture of the two characteristic airstreams of high and low $\theta_E$, or from the mixed layer further to the west which has an intermediate $\theta_E$.

Figure 7a shows the plot of the surface mesonet SP at 1900 MDT. No unmodified surface air remains [the gust front has crossed the dense mesonet (Fig. 2)], and the downdraft air SP are scattered along the same evaporation line with $\theta_E \sim 333.1 \pm 2.6$ K. The spread along the $\theta_E$ moist adiabat corresponds again to evaporation of from ~3 to 6 g kg$^{-1}$ into air with initial SP where the EL and ML intersect (the same point as in Fig. 6b). Although a wide spread in the evaporation into the downdraft air has occurred, the spread in $\theta_E$ is rather small considering the range initially present between the two airstreams (see Section 6d). The spread in evaporation corresponds to a spread in $\theta$ from ~306 to 299 K. This is highly structured spacially. The air close behind the spreading gust front has $\theta \sim 306$ K, but $\theta$ decreases to below 299 K 50 km behind the surface gust front (Fig. 5).

Figure 7b shows the pattern of mesonet SP at 2000 MDT. The surface potential temperatures have on average dropped a little further and there has been a shift towards a lower $\theta_E$. Two populations have

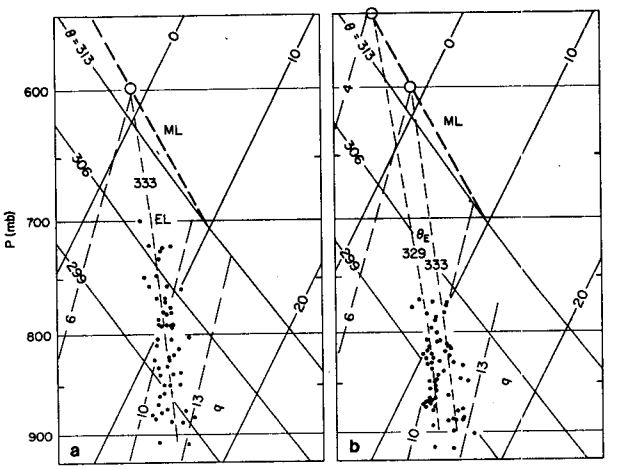


FIG. 7. As in Fig. 6 but of surface mesonet at (a) 1900 and (b) 2000 MDT.

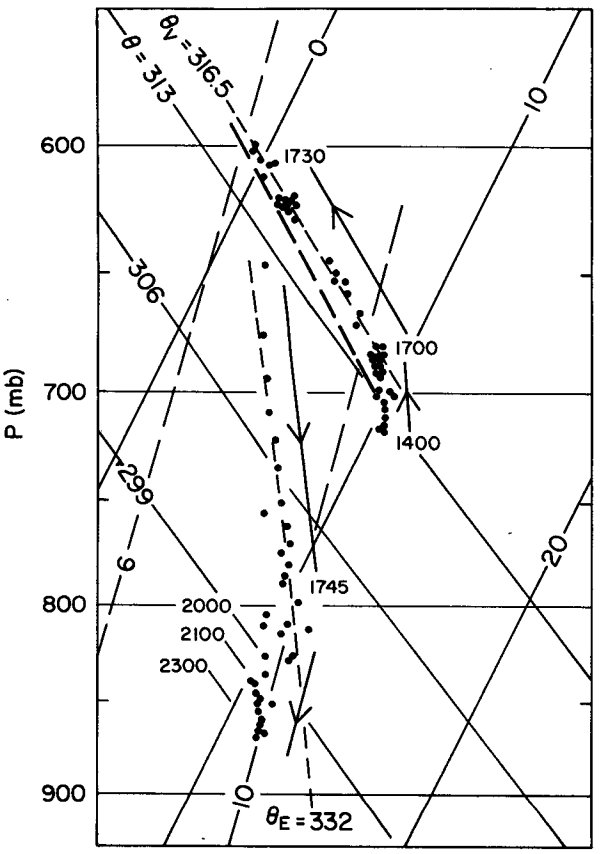


FIG. 8. Time sequence from 1400 to 2300 MDT of surface SP from PAM station 8 (location marked on Fig. 1).

been plotted, and correspondingly two evaporation lines drawn ($\theta_E$ = 329 and 333 K). The open circles are SP for stations in the southeast of the mesonet and these scatter along $\theta_E \sim$ 333 K (or slightly greater) as in Fig. 7a. The solid circles lie mainly to the north and northeast of the mesonet where downdraft air of lower $\theta_E$, $\theta$ has now reached the network, probably from the decay of the earlier cells to the northeast. The air in the southeast is probably the outflow from the later development which took place there between 1800 and 1900 MDT (Fig. 2).

### *b. Single station time sequence*

For comparison with the area distribution diagrams (Section 6a) and aircraft gust front traverses (Section 6c), we present in Fig. 8 the time series of SP from a single PAM station (labelled 8 in Fig. 1). The data are minute averages: values are plotted every 10 min from 1400 to 1700 MDT and 1750 to 2300 MDT, and every minute from 1700 to 1745 as the gust front approaches and passes the station. This one station shows the features of many of the preceding diagrams. From 1400 to 1700 MDT the surface SP has a trend towards higher $\theta$ and lower $q$ similar to that shown by the subcloud aircraft data (Fig. 4). Thirty minutes before the gust front, the surface wind turns towards the southwest and ($\theta_E$, $q$) drop rapidly. The SP path approximately traces the mixing line of Figs. 3 and 6a. This drier air is probably advected in from the west, but it could also descend from above and ahead of the gust front since the SP structure shows constant $\theta_v$ = 316.5 K (dashed line). This deserves further study.

With the passage of the gust front (peak winds 28 m s$^{-1}$) the SP falls rapidly down an EL of $\theta_E$ = 332 K to a saturation level about 100 mb above the surface. The general trend after sunset from 2000 to 2300 is probably due to radiative cooling which moves the SP down a line of constant $q$.

Several other PAM stations show a similar trend of SP up a mixing line ahead of the gust front, while others show a rapid transition from high $\theta$, $q$, $\theta_E$ to an evaporation line structure with the arrival of the gust front. This suggests that the transition shown in

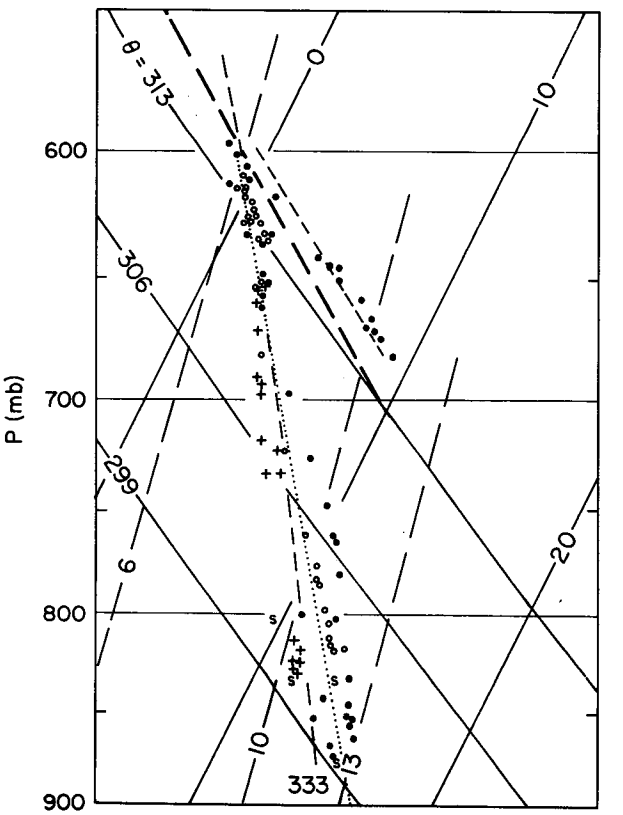


FIG. 9. SP structure from three aircraft soundings through or behind the surface gust front. Dots are first descent sounding through the gust front, open circles ascent in the outflow, and crosses descent sounding into Miles City. Symbols S denote SP of surface air from nearest mesonet stations to soundings. The $\theta_E$ = 333 K evaporation line and the mixing line through C on Fig. 4 are shown dashed. The dotted line is the $\theta_{ESV}$ = 340 K isopleth (see Section 6f).

Fig. 8 from 1730 to 1745 represents different amounts of evaporation rather than simply mixing at the gust front boundary.

### c. *Aircraft gust front traverses*

The NCAR Queen Air N306D made gust front traverses while making soundings just before landing. These show both a vertical profile of ($\theta$, $\theta_E$) in the outflow as well as an SP structure which is similar to Figs. 7, 8. Figure 9 shows the three soundings on an SP diagram, starting at 1945 MDT. Ahead of the gust front, the ML structure corresponding to the final time on Fig. 4 appears (dashed). The aircraft then enters air modified by the evaporation of rain which has $\theta_E \sim 333$ K (dashed) and a lower $\theta_v$. The heavy dots show SP in the first descent sounding from 690 mb to 912 mb (coordinates near [60, 0 km] at 1957 MDT), the open circles the following ascent from 910 to 822 mb, and the crosses the descent into landing at Miles City from 822 mb. The symbols S denote surface values from the mesonet stations nearest to the aircraft at the bottom of its soundings: the agreement between aircraft and the local surface data is good. The soundings to the east follow a higher $\theta_E \sim 337$ K than the descent near Miles City ($\theta_E \sim 331$ K). Despite this spacial variation which is also visible in the mesonet data (Fig. 7b), the general SP structure following an evaporation line of $\theta_E \sim 333$ K is very similar to that shown in Figs. 7a, 7b, for the surface data. The dotted line (a virtual potential temperature isopleth for cloudy air) also fits the data well, and is discussed in Section 6f.

Despite the relatively small variations in $\theta_E$, the vertical variation of $\theta$ is large. Downdraft air has completely restratified the atmosphere. Figure 10 shows the vertical profiles of $\theta$ from the aircraft soundings. The fall in $\theta$ between 760 and 850 mb is only a few degrees: the very cold ($\theta < 306$ K) 'density current' outflow (see, for example, Charba, 1974; Miller and Betts, 1977) is quite shallow—only about 300 m deep.

### d. *Possible origin of downdraft air and evaporation line*

The mesonet surface stations (Figs. 6, 7, 8) and the aircraft gust front traverses (Figs. 9) all show an evaporation line structure with $\theta_E \sim 333$ K behind the gust front from the major storm, covering a large horizontal area and a deep layer. The source of this low $\theta_E$ downdraft air is of importance. Clearly, this needs further kinematic and dynamic study using the Doppler radar data, but a thermodynamic analysis suggests some possibilities. Air is approaching the storm at low levels from the southeast with approximately a two-layer structure in the vertical: dry air of $\theta_E \sim 323$ K overlies moist air of $\theta_E \sim 347$ K (Fig. 3) with little air of intermediate $\theta_E$. High $\theta_E$ values from cold downdrafts are seen only briefly at the surface after the first showers (Fig. 6a), and very low values of $\theta_E < 325$ K corresponding to descent with evaporation of the dry upper layer in undiluted downdrafts are not recorded at any surface station. If the air in the extensive outflow originated ahead of the storm to the southeast then extensive mixing must occur between the initially distinct air masses to generate the observed large volumes of intermediate $\theta_E$ air. A mechanism exists for this, which has received little attention. Evaporation of small amounts of precipitation readily drive downward mixing of dry air in the vicinity of the storm, because the slope of the mixing line is close to the $\theta_v$ isopleth (Fig. 3), and, in this case, may have decreasing stability with time (Fig. 4). Figure 3 illustrates that the evaporation of only 0.63 g kg$^{-1}$ of precipitation into $\theta_E = 325$ K air will drop the $\theta_v$ of its SP off the mixing line (down a moist adiabat) below that of the subcloud layer ($\theta_v \sim 315$ K) and promote downward mixing.

The other possible source of the outflow air with $\theta_E \sim 333$ K is the drier mixed layer air to the west which has comparable $\theta_E$ and is approaching the storm from the west. It could ascend over the advancing gust front and feed a downdraft circulation as it enters a precipitation area.

It is clear that the origin of the downdraft inflow deserves further kinematic and dynamic study. The significant observational fact is that it is rather homogeneous in $\theta_E$ (much more so than the ambient atmosphere ahead of the storm). The spread of SP along an evaporative line implies more or less evaporation of precipitation during its downdraft descent. The coolest air naturally stratifies nearest the surface.

### e. *Estimation of downdraft outflow statistics*

Downdraft outflow statistics can be readily computed using the SP analyses. We shall take Fig. 7b as a representative example. We may assume the SP of air entering the downdraft circulation originally lay at the intersection of the $\theta_E$ isopleth and the mixing line (denoted by an open circle) above. The differences in $q$ values between this point and the observed outflow SP are evaporation amounts. The downdraft data points in Fig. 7b, corresponding to air at the surface, have experienced a mean evaporation $E = 5.8 \pm 0.9$ g kg$^{-1}$. Figure 10 can be converted into an approximate profile of evaporation with height by differencing from $\theta = 315$ K and dividing by $L/C_p = 2.5$°K kg g$^{-1}$. From a budget viewpoint the evaporation into the outflow corresponds to a mean value of 3 g kg$^{-1}$ over a pressure depth $\sim 120$ mb.

Air that has reached the surface in Fig. 7b has probably descended about 250 mb from a layer above cloud base. Betts and Silva Dias (1979) and Betts (1982b) showed, with a simple one-dimensional model, that a downdraft outflow subsaturation pa-

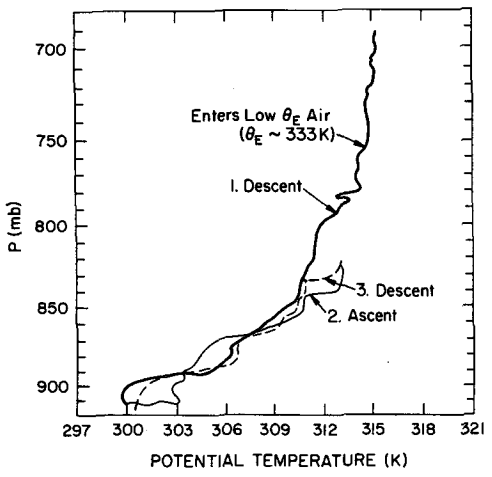


FIG. 10. Potential temperature profiles corresponding to soundings in outflow air (Fig. 19).

rameter ($\mathcal{P} = p_{SL} - p$) approaches an evaporation pressure scale $\pi_E$ associated with droplet spectrum and downdraft speed, if the downdraft descent is much greater than $\pi_E$ mb. $\mathcal{P}$ and by inference $\pi_E$ show considerable variation in Fig. 7b with a mean value 80 ± 36 mb. In a study of tropical cumulonimbus Betts and Silva Dias (1979) found a similar range but a smaller mean value of $\pi_E \sim 55$ mb.

### *f. Comparison with tropical downdraft airflows over land*

Betts (1976b) did a mean analysis of downdraft outflow structure and evaporation for a set of 13 tropical cumulonimbus systems. Converted to an SP representation, these show a similar structure to this High Plains storm. Figure 11 shows that the mean cumulonimbus inflow SP structure (solid circles) lie close to the dashed mixing line (except for the surface SP). The open circles are the SP of the tropical outflow: they show a structure which is close (but slightly unstable) to a moist adiabat of $\theta_{ES} = 341$ K. The general similarity to Figs. 3 and 9 is apparent although the tropical inflow mixing line has a much more stable $\theta_V$ slope than that of the severe storm.

A simple model which represented this transformation in terms of mixing and evaporation processes in the downdraft circulation was given in Betts (1976b). Inflow SP between A and B (the subcloud layer) in the model were assumed to ascend in updrafts, while air from the layer initially above cloud base, with SP from B to C, was assumed to descend in downdrafts with mixing and evaporation to give the downdraft outflow SP structure DE. Mixing within the downdraft circulation reduces the spread of $\theta_E$ while evaporation changes saturation level $p_{SL}$. The inset to Fig. 11 (on right) linearizes BC and DE to give a schematic for this transformation. Although the mixing and evaporation processes occur simultaneously we may on an SP diagram consider them sequentially, and here it is convenient to consider mixing first. Mixing within the downdraft circulation reduces the spread of $\theta_E$ and following Betts (1976b) we may quantify this with a parameter $\alpha$, where $0 < \alpha < 1$. In this case $\alpha = 0$ corresponds to no mixing and $\alpha = 1$ to complete mixing of the layer to constant $\theta_E$. In Fig. 11 the reduction in the spread of $\theta_E$ (and $p_{SL}$) from BC to B′C′ by mixing gives a value $\alpha \sim 0.7$. Evaporation of precipitation only changes $p_{SL}$ and schematically moves C′ to E and B′ to D. This corresponds to a gradient of evaporation from 3.4 g kg$^{-1}$ ($\Delta p_{SL}$ = 165 mb) into air in the downdraft outflow near the surface to only 1.4 g kg$^{-1}$ ($\Delta p_{SL}$ = 65 mb) into outflow air exiting the storm 130 mb above the surface (which was the mean inflow cloud base level).

We may draw a similar schematic for the severe storm case (Fig. 12). The heavy dashed mixing line corresponds to the severe storm inflow (Fig. 3) with $\theta_E$ ranging from ~347 K in the deep subcloud layer to ~323 K in the dry layer above. The dashed evaporation line of $\theta_E$ = 333 K is drawn as representative of the SP of the deep downdraft outflow (see Figs. 7 and 9). This corresponds to $\alpha \sim 1$, well mixed in $\theta_E$. Downdraft air exiting the storm near the surface has experienced an evaporation of ~5.8 g kg$^{-1}$ corresponding to $\Delta p_{SL} \sim 260$ mb. However, as discussed in Section 6d, it is not clear what air is

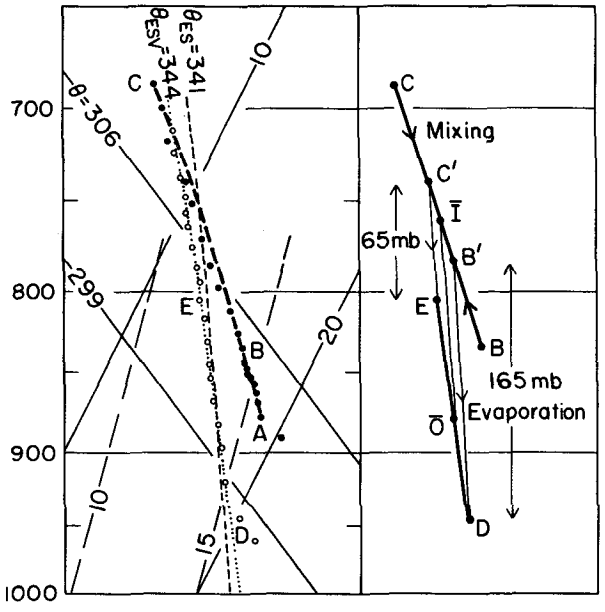


FIG. 11. Mean SP structure of tropical cumulonimbus inflow (ABC) and downdraft outflow (DE). The mixing line AC is shown dashed. On the right is a schematic showing the mixing and evaporation model of Betts (1976b): the light lines, C′E, ĪŌ, and B′D are moist adiabats, and Ī, Ō are SP corresponding to the mean downdraft inflow and outflow.

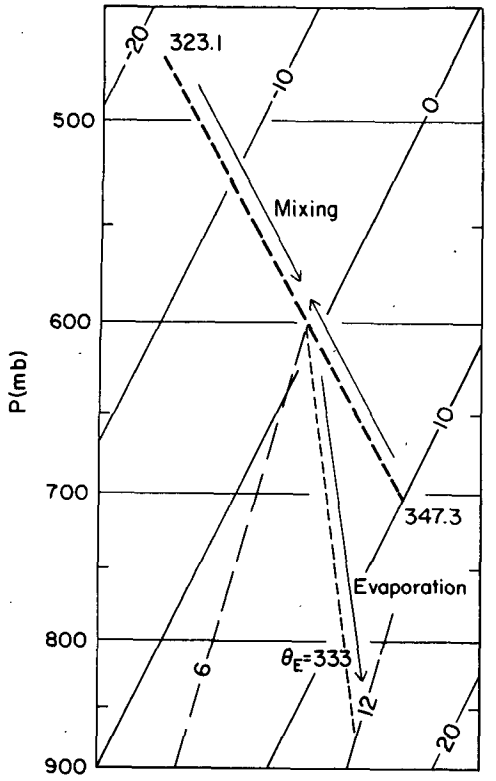


FIG. 12. Schematic summarizing the downdraft process in the severe storm. The mixing line from Fig. 3 and evaporation line from Fig. 9 are shown dashed.

incorporated into the downdraft and hence the range of SP (and $\theta_E$) entering the mixing in Fig. 12 is not known.

One unexplained aspect of Fig. 11 however is that the downdraft outflow SP away from the surface lie very close to a virtual potential temperature isopleth for cloudy processes: $\theta_{ESV}$ = 344 K (Betts, 1983) is shown dotted. Betts (1982a) showed examples of deep convective equilibrium atmosphere whose temperature and SP structure approached a $\theta_{ESV}$ isopleth in the lower troposphere, and gave a plausible explanation in terms of stability to cloudy updrafts. It is less obvious however why downdraft outflows driven by evaporating precipitation should approach a $\theta_{ESV}$ structure. It may be for the tropical case that some sort of equilibrium is reached and deep convection ceases once sufficient boundary layer air has been processed to modify the SP profile back to a $\theta_{ESV}$ isopleth, which is stable to cloudy updrafts. Indeed Betts (1973) estimated from a similar tropical data set that the cumulonimbus ceased after processing only about half the subcloud layer air. For the severe storm the dotted $\theta_{ESV}$ = 340 K isopleth on Fig. 9 is also a reasonable fit to the aircraft profile data. However the passage of a severe storm may not leave the atmosphere close to a deep convective equilibrium structure (Fritsch *et al.*, 1976). This needs further study.

## 7. Conclusions

In this paper a study of the boundary layer thermodynamics of the inflow to and outflow from a severe thunderstorm which passed through the CCOPE network near Miles City, Montana on 1 August 1981 is presented. Its main focus is a new analysis procedure using air parcel saturation point.

In the air mass ahead of the severe storm all data sets (aircraft, upper air soundings and surface mesonet) stratified close to one basic mixing line structure (Section 5). This suggests that SP methods may be very useful in intercomparing and merging, mesoscale data sets from diverse spacial and temporal sampling systems. It also suggests that this mixing line structure may be a useful way to characterize the thermodynamics of the thunderstorm environment. As an appendix we show how the evolution of the subcloud layer ahead of the severe storm can be represented on an SP budget diagram.

The main storm outflow at low levels has a distinct and different thermodynamic structure, in which the aircraft and surface mesonet data sets now stratify along an evaporation line (Section 6). This homogeneity of the severe storm low-level outflow in terms of $\theta_E$ is a little surprising and certainly deserves further study.

The SP analysis of the transformation of the boundary layer focusses attention on two important processes in the thunderstorm thermodynamics: mixing which reduces the spread of $\theta_E$ and saturation level between different air parcels (while maintaining a mixing line structure), and the evaporation of falling precipitation which approximately conserves $\theta_E$, but changes saturation level. The transformation from one characteristic state to another can then be explored in terms of characteristic parameters for mixing and evaporation.

This view of the storm's boundary layer thermodynamics as a transformation from a mixing line to an evaporation line structure suggests a simple parameterization of the thermodynamic effects of thunderstorms in numerical models. A comparison with a set of tropical thunderstorm shows that the concept may have some generality. Work on this is in progress.

Data analysis on the mesoscale and the intercomparison of different data systems should find this analysis tool valuable. Kinematic studies of storm mesoscale structure using multiple Doppler radars may also find the SP analysis useful as a tracer on the thermodynamic transformations involved.

*Acknowledgments.* The CCOPE data analysis of this paper was performed while the author was a visiting scientist in the Convective Storms Division

of the National Center for Atmospheric Research, supported by the National Science Foundation. The theoretical part of this work was supported by the National Science Foundation, Global Atmospheric Research Program under Grant ATM-8120444. I am grateful to C. A. Knight and reviewers for suggesting improvements, and to Carol Brown for preparing the manuscript.

## APPENDIX

## Subcloud Layer Budget

We show how the thermodynamic budget for the subcloud layer can be compactly represented as the sum of vector changes on a saturation point diagram.

### 1. Budget equation

We may think of the trend **ABC** of the mixed layer SPM as a two-dimensional vector, and following Betts (1983) represent the thermodynamic budgets for the mixed subcloud layer as a vector equation. The radiative flux divergence is here neglected.

$$\frac{\Delta p}{g}\left(\frac{\partial \mathbf{M}}{\partial t}+\mathbf{v}\cdot\nabla\mathbf{M}\right)=\mathbf{F}_0-\mathbf{F}_b, \tag{1}$$

where $\Delta p$ is the pressure thickness of the subcloud layer, $\mathbf{F}_0$, $\mathbf{F}_b$ are the vector thermodynamic fluxes at the surface and cloud-base. Equation (1) has two *independent* component equations, for example, the $\theta$ and $q$ budgets; although in fact it can be projected onto any of the thermodynamic variables to give also the $\theta_E$ and $\theta_V$ budgets (Betts, 1983). We may write (1) in finite difference form as

$$\frac{\Delta p}{g\Delta t}(\Delta\mathbf{M}-\Delta\mathbf{M}_{ad})=\mathbf{F}_0-\mathbf{F}_b, \tag{2}$$

where $\Delta\mathbf{M}$ is the change of $\mathbf{M}$ in the budget time interval $\Delta t$ (the vector **AC** in Fig. 4) and the advective term has been rewritten as an advective change $\Delta\mathbf{M}_{ad}$, defined as

$$-\mathbf{v}\cdot\nabla\mathbf{M}\equiv\partial\mathbf{M}_{ad}/\partial t\equiv\Delta\mathbf{M}_{ad}/\Delta t. \tag{3}$$

### 2. Flux representation using SP vectors

A thermodynamic flux vector can be represented by the product of a mass flux scale ($\omega/g$) and an SP difference ($\Delta\mathbf{S}$), as in Betts (1983).

$$\mathbf{F}\equiv\left(\frac{\omega}{g}\right)\Delta\mathbf{S}. \tag{4}$$

This assumes that both heat and moisture have similar transport processes, so that both can be represented using the same velocity or mass flux scale. Using (4) *fluxes* can then be plotted as SP vector *differences* on a thermodynamic diagram.

It is convenient here to use the mass flux scale from (2) for both fluxes.

$$\frac{\omega}{g}\equiv\frac{\Delta p}{g\Delta t}. \tag{5}$$

Substituting (5), we represent the fluxes by SP differences

$$\mathbf{F}_0=\left(\frac{\omega}{g}\right)\Delta\mathbf{S}_0;\quad \mathbf{F}_b=\left(\frac{\omega}{g}\right)\Delta\mathbf{S}_b, \tag{6}$$

so that (2) becomes a simple SP vector sum

$$\Delta\mathbf{M}=\Delta\mathbf{S}_0-\Delta\mathbf{S}_b+\Delta\mathbf{M}_{ad}. \tag{7}$$

The insert to Fig. 4 shows the vector diagram for two sets of assumptions (see Section 5b of this appendix).

### 3. Bowen ratio of a flux vector

Every vector $\Delta\mathbf{S}$ has components $\Delta\theta$, $\Delta q$, so that because of (4), which relates $\Delta\mathbf{S}$ to a flux vector, we may define a Bowen ratio $\beta$ related to the $C_p\theta$ and $Lq$ fluxes

$$\beta=\frac{C_p\Delta\theta}{L\Delta q}. \tag{8}$$

Thus every SP difference $\Delta\mathbf{S}$ has an associated Bowen ratio. Figure A1 shows a Bowen ratio rose drawn for $\mathbf{M}$ of 10°C, 700 mb representative of the mixed layer budgets in this paper (there is a variation with $\mathbf{M}$). Two schematic vectors are drawn: a surface vector ($\mathbf{F}_0$, with $\beta\sim 1.5$, representing the fluxes from a warmer, moister surface, and a cloudbase flux vector $-\mathbf{F}_b$ representing the downward mixing of warmer, drier air from the cloud-layer. We see that the slope of the mixing line in Fig. 4 has therefore an associated Bowen ratio (here −0.19), because it couples the heat and moisture fluxes at cloud-base.

We can see from Fig. A1 that surface values of

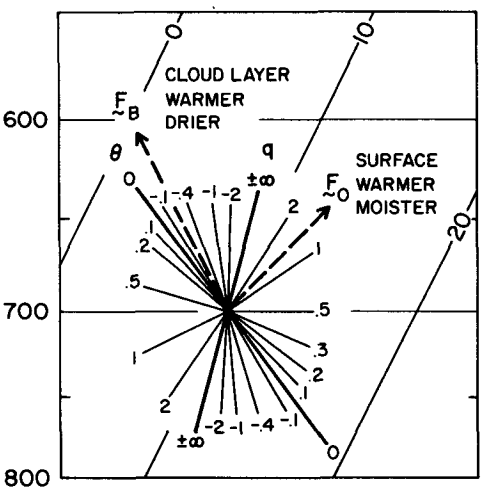


FIG. A1. Bowen ratio $\beta$ associated with slope of an SP vector difference, drawn with central point $\mathbf{M}$ of 10°C and 700 mb representative of Fig. 4. Schematic surface and cloud-base flux vectors are drawn corresponding to $\beta=1.5$ and −0.2 representative of the budget in Fig. 4.

Bowen ratio $\beta < 0.5$ tend to lower cloud-base (the saturation level of **M**) whereas $\beta > 0.5$ cause rising cloud-base. This critical value of $\beta$ increases with decreasing mixing ratio. The entrainment from the cloud layer above ($\mathbf{F}_b$) however tends always to raise the height of cloud-base. Over the ocean where surface Bowen ratios are small (~0.1) cloud-base height can remain constant because these two terms balance, whereas over land cloud-base rises during daytime because surface values of $\beta$ are typically larger.

## 4. Schematic subcloud layer budget

Surface heat and moisture fluxes are not yet available from the CCOPE experiment. Nonetheless by estimating them we can construct a qualitative SP vector diagram for the subcloud layer budget which shows the importance of horizontal advection. We shall first show that if horizontal advection is neglected, the budget requires unrealistic surface fluxes. The mass flux scale is

$$\omega/g = \Delta p/g\Delta t = 0.14 \text{ Kg m}^{-2} \text{ s}^{-1}$$

for $\Delta p = 210$ mb, $\Delta t = 4.25$ h (the time associated with the change from **A** to **C**).

### *a. Neglecting horizontal advection*

The dashed triangle **AFC** in the insert to Fig. 4 shows this budget. Representing SP by letters, we may rewrite (7) (neglecting $\Delta \mathbf{M}_{ad}$) as

$$(\mathbf{C} - \mathbf{A}) = (\mathbf{F} - \mathbf{A}) + (\mathbf{C} - \mathbf{F}). \quad (9)$$

The slope of (**C** − **F**) is known: it is that of the mixing line above cloudbase, which we shall take as the line through **B** at 1600 MDT. We have only to assume a value for the surface Bowen ratio to close the vector triangle. No good estimates of $\beta$ over the network are available, so a rough estimate of 1.5 is used here. (Estimates based on the short-term fluctuations of $\theta$, $q$ at PAM stations give values in the range 1–2). However, the surface sensible and latent heat fluxes corresponding to (**F** − **A**) are (511 and 351) W m$^{-2}$, which are much too large for afternoon data over land, and no change in $\beta$ would give realistic surface fluxes.

### *b. Budget based on estimated surface fluxes*

The vector diagram **ADEC** is based on surface flux estimates, and is likely to be more realistic. Equation (7) can be rewritten as

$$(\mathbf{C} - \mathbf{A}) = (\mathbf{D} - \mathbf{A}) + (\mathbf{E} - \mathbf{D}) + (\mathbf{C} - \mathbf{E}) \quad (10)$$

in which **D** − **A** corresponds to a surface sensible and latent heat flux of 293 W m$^{-2}$. This was estimated from a surface energy budget. Auer and White (1983) constructed net radiation curves for the CCOPE area using aircraft data. A ground storage of 20% of the net radiation was assumed and the derived total sensible and latent heat flux was partitioned with the same assumed Bowen ratio, $\beta = 1.5$. Figure 4 shows that this flux is small compared with the observed change **C** − **A** of the mixed layer.

In Eq. (10) **E** − **D** corresponds to the cloud-base sensible and latent heat fluxes. It is parallel to the dashed mixing line through **B**, taken as representative of the budget time period. Its slope and hence Bowen ratio is fixed by the mixing line slope (here $\beta \approx -0.19$). The magnitude of **E** − **D** was fixed by applying the closure condition on the ratio of cloud-base to surface $\theta_v$ flux, frequently used in mixed layer models (Betts, 1976a):

$$k = -F_{b\theta v}/F_{0\theta v} = -0.2. \quad (11)$$

Graphically this means that the ratio of the projections of **E** − **D** and **D** − **A** onto the $\theta_{vu}$ isopleths is −0.2.

The term **C** − **E**, corresponding to the advective change of **M**, is found as the residual. It is clear that regardless of the uncertainties in the surface fluxes, advection plays an important role in the subcloud layer thermodynamic budget.

Table A1 summarizes the SP coordinates of **ACDEF** in Fig. 4. The ratio of $\theta$, $q$, $\theta_E$, $\theta_{vu}$ differences in this table is the ratio of the associated fluxes. For example, the water vapor flux through cloud base, associated with vector **DE**, is nearly three times the surface vapor flux, associated with **AD**.

The SP vector diagram gives a compact representation of the subcloud layer budget, although the use of a $\theta$ budget implies a small approximation associated with the neglect of kinetic energy dissipation (Betts, 1974). The aircraft data below cloud base gives the subcloud SP change and the ratio of the cloud-base fluxes (five parameters). By specifying three other parameters (two surface fluxes and $k$), we are able here to specify the budget in terms of four SP, **ADEC** (eight independent coordinates). In the absence of advection, we need only specify one extra parameter to determine a budget triangle **AFC**. (Surface Bowen ratio was chosen in a, but the resulting budget gives unrealistic surface fluxes, since advection here is a major term.)

TABLE A1. SP Coordinates in Fig. 4 insert.

| | $T_{SL}$ | $p_{SL}$ | $\theta$ | $q$ | $\theta_E$ | $\theta_{vu}$ |
|---|---|---|---|---|---|---|
| A | 10.4 | 729 | 310.4 | 10.95 | 344.0 | 312.5 |
| C | 8.7 | 608 | 314.7 | 10.47 | 347.5 | 316.7 |
| D | 10.7 | 721 | 311.7 | 11.30 | 346.6 | 313.8 |
| E | 9.0 | 702 | 312.2 | 10.34 | 344.2 | 314.1 |
| F | 11.2 | 707 | 314.0 | 11.93 | 351.5 | 316.3 |

## REFERENCES


Auer, A. H., and J. M. White, 1983: Boundary layer perturbations associated with terrain, physiographical and topographical influences in CCOPE. Res. Rep., Dept. Atmos. Sci., University of Wyoming, Laramie, 57 pp.

Betts, A. K., 1973: A composite cumulonimbus budget. *J. Atmos. Sci.*, **30,** 597–610.

——, 1974: Further comments on "A comparison of the equivalent potential temperature and the static energy." *J. Atmos. Sci.*, **31,** 1713–1715.

——, 1976a: Modeling subcloud layer structure and interaction with a shallow cumulus layer. *J. Atmos. Sci.*, **33,** 2363–2382.

——, 1976b: The thermodynamic transformation of the tropical subcloud layer by precipitation and downdrafts. *J. Atmos. Sci.*, **33,** 1008–1020.

——, 1982a: Saturation point analysis of moist convective overturning. *J. Atmos. Sci.*, **39,** 1484–1505.

——, 1982b: Cloud thermodynamic models in saturation point coordinates. *J. Atmos. Sci.*, **39,** 2182–2191.

——, 1983: Thermodynamics of mixed stratocumulus layers: Saturation point budgets. *J. Atmos. Sci.*, **40,** 2655–2670.

——, and M. F. Silva Dias, 1979: Unsaturated downdraft thermodynamics in cumulonimbus. *J. Atmos. Sci.*, **36,** 1061–1071.

Browning, K. A., and F. H. Ludlam, 1962: Airflow in convective storms. *Quart. J. Roy. Meteor. Soc.*, **88,** 117–135.

Carlson, T. N., and F. H. Ludlam, 1968: Conditions for the occurrence of severe local storms. *Tellus,* **20,** 203–226.

——, S. G. Benjamin, G. S. Forbes and Y.-F. Li, 1983: Elevated mixed layers in the regional severe storm environment: Conceptual model and case studies. *Mon. Wea. Rev.*, **111,** 1453–1473.

Charba, J., 1974: Application of gravity current model to analysis of squall-line gust front. *Mon. Wea. Rev.*, **102,** 140–156.

Fritsch, J. M., C. F. Chappell and L. R. Hoxit, 1976: The use of large-scale budgets for convective parameterization. *Mon. Wea. Rev.*, **104,** 1408–1418.

Goff, R. C., 1976: Vertical structure of thunderstorm outflows. *Mon. Wea. Rev.*, **104,** 1429–1440.

Knight, C. A., 1982: The Cooperative Convective Precipitation Experiment (CCOPE) 18 May–7 August 1981. *Bull. Amer. Meteor. Soc.*, **63,** 386–398.

——, and P. Squires, 1982: Hailstorms of the Central High Plains. *The National Hail Research Experiment, Vol. I,* C. A. Knight and P. Squires, Eds., National Center for Atmospheric Research in association with Colorado Associated University Press, 282 pp.

Ludlam, F. H., 1963: *Severe Local Storms. Meteor. Monogr.,* No. 27, Amer. Meteor. Soc., Boston, 1–30 pp.

——, 1980: *Cloud and Storms.* Pennsylvania State University Press, 405 pp.

Miller, M. J., and A. K. Betts, 1977: Travelling convective storms over Venezuela. *Mon. Wea. Rev.*, **105,** 833–848.

Paluch, I. R., 1979: The entrainment mechanism in Colorado cumuli. *J. Atmos. Sci.*, **36,** 2467–2478.

Zipser, E. J., 1969: The role of organized, unsaturated convective downdrafts in the structure and rapid decay of an equatorial disturbance. *J. Appl. Meteor.*, **8,** 799–814.

——, 1977: Mesoscale and convective scale downdrafts as distinct components of squall-line structure. *Mon. Wea. Rev.*, **105,** 1568–1589.